

## Fully filling-controlled pyrochlore ruthenates: Emergent ferromagnetic-metal state and geometrical Hall effect

Ryoma Kaneko,<sup>1,2</sup> Kentaro Ueda<sup>1,\*</sup>, Shiro Sakai<sup>2</sup>, Yusuke Nomura<sup>2</sup>, Marie-Therese Huebsch<sup>2</sup>,  
Ryotaro Arita<sup>1,2</sup> and Yoshinori Tokura<sup>1,2,3</sup>

<sup>1</sup>Department of Applied Physics, University of Tokyo, Tokyo 113-8656, Japan

<sup>2</sup>RIKEN Center for Emergent Matter Science, Wako 351-0198, Japan

<sup>3</sup>Tokyo College, University of Tokyo, Tokyo 113-8656, Japan



(Received 7 March 2021; revised 15 April 2021; accepted 20 April 2021; published 17 May 2021)

Carrier doping to the Mott insulator is essential to produce highly correlated metals with emergent properties. The pyrochlore ruthenates  $\text{Pr}_2\text{Ru}_2\text{O}_7$  (Ru  $4d$  electron number  $n = 4$ ) and  $\text{Ca}_2\text{Ru}_2\text{O}_7$  ( $n = 3$ ) are a Mott insulator and a magnetic bad metal, respectively, due to the strong electron correlation. We investigate magnetotransport properties of  $(\text{Pr}_{1-x}\text{Ca}_x)_2\text{Ru}_2\text{O}_7$  in a whole band-filling range,  $0 \leq x \leq 1$ . With increasing hole doping  $x$ , the system undergoes an insulator-metal transition. When  $\text{Ca}_2\text{Ru}_2\text{O}_7$  is doped with electrons ( $0.5 < x < 0.9$ ), the enhanced coupling among Ru  $4d$  spins produces a ferromagnetic-metal phase with a large anomalous-Hall angle up to 2%. We discuss the electronic phase transitions in  $(\text{Pr}_{1-x}\text{Ca}_x)_2\text{Ru}_2\text{O}_7$  in view of Hund's metal.

DOI: [10.1103/PhysRevB.103.L201111](https://doi.org/10.1103/PhysRevB.103.L201111)

Mottness, a feature related to electron localization driven by on-site Coulomb repulsion  $U$ , is a key to emergent properties in strongly correlated electronic systems. The systematics of Mottness or related metal-insulator transition (MIT) has been intensively studied in  $3d$ -electron transition-metal oxides, where the bandwidth and band filling can be systematically tuned via chemical doping or applying hydrostatic or chemical pressure [1]. Along with the variation of  $U$  and band filling, versatile magnetoelectronic phenomena such as high-temperature superconductivity [2] and colossal magnetoresistance [3] have been discovered in those systems, generally followed by MITs. Besides the Mottness characterized by  $U$ , recent studies also emphasize the importance of Hund's coupling  $J_H$  [4,5]. Notably,  $J_H$  affects the correlated electron system in two different manners: (i) the partial screening of  $U$  and the modification of the critical  $U$  for the MIT and (ii) the reduction of the coherent scale of quasiparticles via unscreened spin fluctuation. These effects of  $J_H$  may lead to a highly correlated non-Fermi-liquid-like state, a so-called Hund's metal [6–12]. Those Hund's metal features are expected to dominate  $4d$  and  $5d$  electron systems, where the scales of  $U$  and  $J_H$  are sufficiently close. These systems attract interest also in light of topological properties derived from electronic bands reconstructed by strong spin-orbit coupling (SOC)  $\lambda$  [13]. The interplay of  $J_H$  with  $\lambda$  is nontrivial because  $\lambda$  enhances the orbital mixing, whereas  $J_H$  tends to decouple spin and orbital degrees of freedom [14]. Thus, the  $4d$ - and  $5d$ -electron systems attract current interest, where plural inter- and intra-atomic interactions cooperate or compete with each other.

In this context,  $R_2\text{Ru}_2\text{O}_7$  ( $R$  is a trivalent rare-earth ion and Y) provides an important arena for research. In  $R_2\text{Ru}_2\text{O}_7$ ,  $R$  and Ru ions respectively form pyrochlore lattices composed of corner-sharing tetrahedrons displaced by half a unit cell from each other [15]. In the ionic picture on the Mott insulator, local trigonal distortion around  $\text{Ru}^{4+}$  splits the valence  $t_{2g}$  orbitals into doubly degenerate  $e'_g$  and nondegenerate  $a_{1g}$  orbitals; two of the four Ru  $4d$  electrons fully occupy the  $a_{1g}$  orbital, and the other two fill half of the  $e'_g$  orbitals with their spins aligned by Hund's rule coupling [Fig. 1(b)]. As a result,  $R_2\text{Ru}_2\text{O}_7$  has the  $S = 1$  spin ordered antiferromagnetically at low temperatures, while it is electrically an insulator at all temperatures and for all  $R$  ( $= \text{Pr-Lu}$ ) [16,17]. The neutron diffraction studies suggest antiferromagnetic magnetic structures in  $R_2\text{Ru}_2\text{O}_7$ , the details of which depend on the  $R$   $4f$  moments with different magnetic anisotropies [15,17–21]. The  $R = \text{Pr, Nd, or Ho}$  compounds, whose  $f$  moments have strong uniaxial anisotropy with respect to the local  $\langle 111 \rangle$  axes, are especially important because these antiferromagnetic moments can order in a noncoplanar all-in-all-out structure [Fig. 1(a)] [16,17]. The magnetic field along the specific crystal axis can transform the all-in-all-out to the two-in-two-out or three-in-one-out structure, which significantly affects the magnetic and electronic properties [22].

Trivalent  $R$  ions can be replaced by divalent ions  $A$  such as Ca and Cd, accompanied by the oxidization number increasing from  $\text{Ru}^{4+}$  to  $\text{Ru}^{5+}$ . This reduces the number of Ru electrons from four to three. The spin state changes from  $S = 1$  to  $S = 3/2$  [Fig. 1(b)], and the upward shift of the oxygen  $2p$  bands reduces  $U$  and  $J_H$  by enhancing the screening effect. Contrary to  $R_2\text{Ru}_2\text{O}_7$ , which is an antiferromagnetic Mott insulator,  $\text{Ca}_2\text{Ru}_2\text{O}_7$  and  $\text{Cd}_2\text{Ru}_2\text{O}_7$  show bad metallic behavior with spin-glass transitions at low temperatures [23,24]. Such contrasting magnetic and electronic characters between the end compounds,  $R_2\text{Ru}_2\text{O}_7$  and  $A_2\text{Ru}_2\text{O}_7$ , imply

\*Corresponding author: ueda@ap.t.u-tokyo.ac.jp

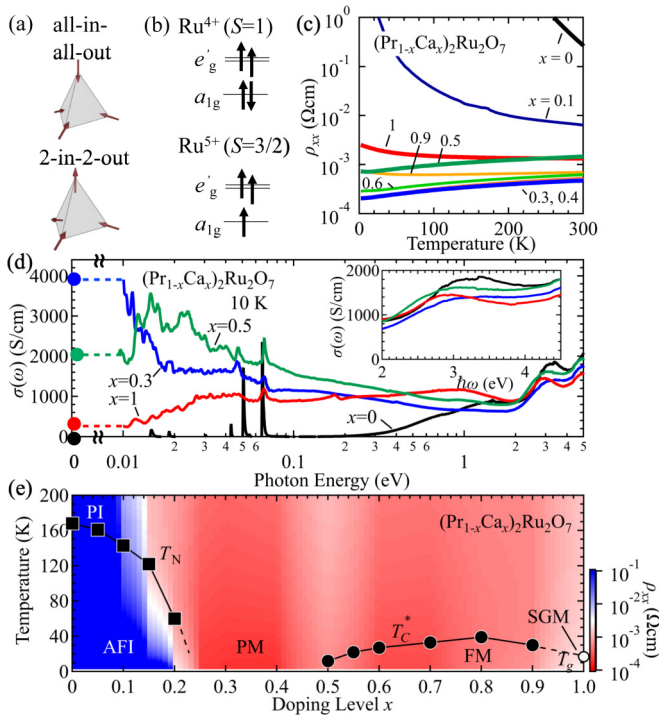


FIG. 1. (a) All-in-all-out and two-in-two-out magnetic structures. (b)  $e'_g$  and  $a_{1g}$  electronic levels and spin states of  $Ru^{4+}$  and  $Ru^{5+}$  in the ionic model. (c) Temperature dependence of resistivity  $\rho_{xx}$  for  $(Pr_{1-x}Ca_x)_2Ru_2O_7$ .  $\rho_{xx}$  of  $x = 0.3$  almost overlaps that of  $x = 0.4$ . (d) Optical conductivity spectra of  $(Pr_{1-x}Ca_x)_2Ru_2O_7$  ( $x = 0, 0.3, 0.5$  and  $1$ ) below a photon energy of  $5$  eV. (e) Contour plots of  $\rho_{xx}$  on the doping level  $x$  versus temperature plane. AFI, PM, FM, and SGM represent the antiferromagnetic insulator, paramagnetic metal, ferromagnetic metal, and spin-glass metal, respectively. Black squares, black circles, and a white circle indicate the magnetic transition temperatures  $T_N$  (antiferromagnetic),  $T_C^*$  (ferromagnetic), and  $T_g$  (spin glass), respectively.

novel phase transitions, as well as related magnetoelectronic phenomena in the intermediate filling-controlled compounds  $(R_{1-x}A_x)_2Ru_2O_7$ .

A previous study [25] focused on the systematic change in charge dynamics of  $R_2Ru_2O_7$  in the course of the bandwidth- and filling-controlled MITs. In the relatively low hole-doped region, the MITs in  $R_2Ru_2O_7$  behave like a canonical filling-controlled Mott transition as in the  $3d$ -electron Mott systems. Nevertheless, the limitation of such a simple framework becomes clear with increasing hole-doping level in the correlated metallic region. As described above, in the  $4d$ -electron systems, the correlated electrons renormalized by the multiorbital effect are anticipated to dominate electronic and magnetic properties in a manner different from the simple case of the doped Mott insulator. Experimentally, Hund's metal regime has been less explored, in particular for pyrochlore compounds. In this study, we investigate the electronic states of the pyrochlore ruthenates systematically in a wide range of filling, which significantly varies the electron correlations induced by  $U$  and  $J_H$ . We successfully synthesized the solid-solution (mixed-crystal) polycrystals of  $(Pr_{1-x}Ca_x)_2Ru_2O_7$  in the whole composition range,  $0 \leq x \leq 1$ . Remarkably, on the

Ca-rich side ( $x \geq 0.5$ ), we find the emergence of ferromagnetism characteristic of Hund's metals. This marks the rare case of a ferromagnetic-metal pyrochlore. Based on the easily spin-polarized tendency of Hund's metal, we also clarify the large geometrical (topological) Hall effects due to the scalar spin chirality emerging from the  $4f$  (Pr)- $4d$  (Ru) spin coupling.

Polycrystalline samples of  $(Pr_{1-x}Ca_x)_2Ru_2O_7$  and  $(Gd_{1-x}Cd_x)_2Ru_2O_7$  were prepared by using a cubic-anvil high-pressure apparatus; detailed procedures are described in the Supplemental Material [26]. Resistivity measurements were conducted by a standard four-probe method, forming the contact with gold wire attached by silver paste. The magnetization was measured by a superconducting quantum interference device magnetometer. The optical reflectivity spectra were measured between  $0.005$  and  $30$  eV using a Fourier transform infrared spectrometer ( $0.05$ – $0.5$  eV) and a grating monochromator ( $0.5$ – $5$  eV). For the Kramers-Kronig analysis to deduce the optical conductivity spectra, the room-temperature vacuum-ultraviolet reflectivity data above  $5$  eV measured at UVSOR (BL-7B), Institute for Molecular Science, were utilized.

Figure 1(d) shows the  $x$  dependence of longitudinal resistivity  $\rho_{xx}$  for  $(Pr_{1-x}Ca_x)_2Ru_2O_7$ . The end compounds,  $Pr_2Ru_2O_7$  and  $Ca_2Ru_2O_7$ , show insulating and bad-metallic behavior, respectively, being typical of the highly correlated electronic state. However, with carrier doping, namely, nominal hole doping into  $Pr_2Ru_2O_7$  or electron doping to  $Ca_2Ru_2O_7$ ,  $\rho_{xx}$  systematically decreases to show metallic temperature dependence, as is typically seen for  $0.3 \leq x \leq 0.9$ . The change in the electronic structure can also be inferred from the optical conductivity spectra for  $x = 0, 0.3, 0.5$ , and  $1$  [Fig. 1(c)]; for  $x = 0$  ( $Pr_2Ru_2O_7$ ) a clear Mott-Hubbard gap of about  $0.3$  eV is observed, while for  $x = 0.3$  a clear Drude tail is discerned below  $0.02$  eV, followed by the broad spectrum in a higher photon energy region ( $0.02$ – $1$  eV). For  $x = 1$  ( $Ca_2Ru_2O_7$ ), the nearly  $\omega$  flat conductivity spectrum dominates below  $1$  eV nearly down to  $0.01$  eV, corroborating the highly incoherent charge dynamics or bad-metal state and hence characterizing the incipient Mott insulator (the peaks at  $0.01$ – $0.07$  eV are due to the optical phonons). Also, characteristic of  $Ca_2Ru_2O_7$  is the redshift of the charge transfer excitation from occupied O  $2p$  to unoccupied (or upper Hubbard bandlike) Ru  $4d$  states, as discerned around  $3$  eV in the inset of Fig. 1(c). This evidences the relative upward shift of the O  $2p$  state due to the high-valence ( $5+$ ) character of the Ru ions in  $Ca_2Ru_2O_7$ .

Figure 1(e) displays a contour plot of  $\rho_{xx}$  together with the assignment of the phases in the plane of  $x$  and temperature  $T$ , where red and blue circles represent the magnetic transition temperatures determined from the anomaly in the temperature dependence of the magnetization. Three distinct phases are discernible in the contour plot. In the small  $x$  region ( $x < 0.3$ ) the antiferromagnetic insulator phase, whose Néel temperature decreases with  $x$ , persists. Then, the paramagnetic-metallic phase appears for  $0.3 \leq x < 0.5$ , and above  $x = 0.5$  a ferromagnetically ordered metallic phase appears below  $40$  K while retaining a metallic value of  $\rho_{xx}$  ( $< 10^{-3} \Omega\text{cm}$ ), as later described in detail. Incidentally, just around  $x = 0.5$  a singular increment of resistivity is discerned

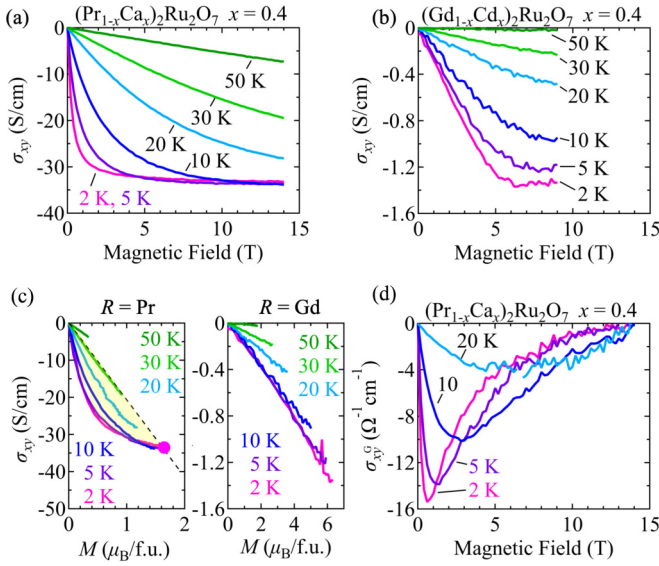


FIG. 2. Magnetic field dependence of Hall conductivity  $\sigma_{xy}$  in the paramagnetic phases of (a)  $(\text{Pr}_{1-x}\text{Ca}_x)_2\text{Ru}_2\text{O}_7$  ( $x = 0.4$ ) and (b)  $(\text{Gd}_{1-x}\text{Cd}_x)_2\text{Ru}_2\text{O}_7$  ( $x = 0.4$ ) at various temperatures. (c)  $\sigma_{xy}$  plotted as a function of magnetization  $M$  for  $(\text{Pr}_{1-x}\text{Ca}_x)_2\text{Ru}_2\text{O}_7$  of  $x = 0.4$  (left) and  $(\text{Gd}_{1-x}\text{Cd}_x)_2\text{Ru}_2\text{O}_7$  of  $x = 0.4$  (right). The yellow shaded region in the left panel highlights the geometrical (topological) Hall term  $\sigma_{xy}^G$  at 2 K. (d) Magnetic field dependence of  $\sigma_{xy}^G$  for  $(\text{Pr}_{1-x}\text{Ca}_x)_2\text{Ru}_2\text{O}_7$  ( $x = 0.4$ ).

in the whole temperature range [Fig. 1(c)], as exemplified in  $\sigma_{xx} \sim \rho_{xx}^{-1}$  at 2 K, as shown in Fig. 4(b). The optical conductivity spectrum for  $x = 0.5$  [Fig. 1(d)] shows the metallic response down to lower energy, yet the pseudogaplike or soft gap feature appears below 0.02 eV with a vanishing Drude component. Though the origin of this insulating tendency around  $x = 0.5$  is unclear at the moment, one possibility is a formation of short-range fluctuating charge order such as an alternate nominal  $\text{Ru}^{4+}/\text{Ru}^{5+}$  configuration on the frustrated pyrochlore lattice, as observed in mixed-valence spinel compounds [27].

Next, we proceed to the magnetotransport properties in the paramagnetic-metal regime. In Fig. 2(a), we show the magnetic field dependence of the Hall conductivity  $\sigma_{xy}$  of  $(\text{Pr}_{1-x}\text{Ca}_x)_2\text{Ru}_2\text{O}_7$  for  $x = 0.4$  at various temperatures.  $\sigma_{xy}$  shows a linear field dependence at high temperatures, but with decreasing temperature below 20 K,  $\sigma_{xy}$  shows a highly field-nonlinear feature, i.e., the anomalous Hall effect (AHE) in a broad context. Because the  $R$  4*f* moments usually begin to polarize at such a low temperature, it is natural to consider that coupling between local  $R$  4*f* moments and conductive Ru 4*d* electrons contributes to the observed AHE. To compare the behavior of  $\sigma_{xy}$  among the  $R_2\text{Ru}_2\text{O}_7$  compounds with a magnetic  $R$  ion with different magnetic anisotropies,  $\sigma_{xy}$  of  $(\text{Gd}_{1-x}\text{Cd}_x)_2\text{Ru}_2\text{O}_7$  for  $x = 0.4$  is shown in Fig. 2(b). Remarkably, the absolute value of  $\sigma_{xy}$  at  $B = 14$  T is an order of magnitude larger for  $(\text{Pr}_{1-x}\text{Ca}_x)_2\text{Ru}_2\text{O}_7$  than for  $(\text{Gd}_{1-x}\text{Cd}_x)_2\text{Ru}_2\text{O}_7$ , although the conductivity  $\sigma_{xx}$  values are both  $> 10^3$  S/cm; the  $\rho_{xx}$  data of  $(\text{Gd}_{1-x}\text{Cd}_x)_2\text{Ru}_2\text{O}_7$  are shown in Fig. S2 [26]. Such a contrast will be attributed to the different  $R$  4*f* moments between  $(\text{Pr}_{1-x}\text{Ca}_x)_2\text{Ru}_2\text{O}_7$  and  $(\text{Gd}_{1-x}\text{Cd}_x)_2\text{Ru}_2\text{O}_7$ ; the former is Ising type with the

magnetic anisotropy along  $\langle 111 \rangle$ , while the latter is Heisenberg type. In  $(\text{Pr}_{1-x}\text{Ca}_x)_2\text{Ru}_2\text{O}_7$ , Ru 4*d* electrons conducting on a noncollinear spin texture composed of Pr 4*f* moments with finite scalar spin chirality (SSC) experience an emergent magnetic field derived from the real-space Berry phase [28]. The resultant transverse response of the electrons is called the topological or geometrical Hall effect (GHE) to distinguish it from the intrinsic (Karplus-Luttinger type) AHE due to SOC; the GHE is now widely observed in frustrated or chiral magnets [29–33].

To analyze the contribution of the  $f$ - $d$  coupling and the resultant GHE, we use the phenomenological relation for the AHE [28],

$$\rho_{yx} = R_0 H + S_A \rho_{xx}^2 M + \rho_{yx}^G, \quad (1)$$

where  $R_0$  and  $S_A$  are the ordinary and anomalous Hall coefficients, respectively. The second term is the  $M$ -linear term mediated by the SOC, including the intrinsic (Karplus-Luttinger) mechanism, and the third term is the geometrical term mediated by the SSC, the source of the GHE in our case. Figure 2(c) plots the  $M$  dependence of Hall conductivity  $\sigma_{xy} = \rho_{yx}/(\rho_{xx}^2 + \rho_{yx}^2)$  for  $(\text{Pr}_{1-x}\text{Ca}_x)_2\text{Ru}_2\text{O}_7$  and  $(\text{Gd}_{1-x}\text{Cd}_x)_2\text{Ru}_2\text{O}_7$  ( $x = 0.4$ ). Here we assume that the ordinary Hall coefficient is negligible ( $|R_0| \sim 10^{-3}$  cm<sup>3</sup>/C, a typical value for metallic pyrochlore oxides [34,35]). For  $(\text{Pr}_{1-x}\text{Ca}_x)_2\text{Ru}_2\text{O}_7$ ,  $\sigma_{xy}$  is not proportional to the magnetization  $M$ , indicating that the SSC originating from the Ising-type Pr 4*f* moments causes the GHE. In contrast, for  $(\text{Gd}_{1-x}\text{Cd}_x)_2\text{Ru}_2\text{O}_7$ , where the Heisenberg-type Gd 4*f* moments produce no static component of SSC,  $\sigma_{xy}$  is almost proportional to  $M$ , i.e., dominated by the conventional AHE.

To extract the contribution of the GHE, we first estimate the  $M$ -linear AHE. At low temperatures below 20 K,  $\sigma_{xy}$  rapidly saturates with increasing magnetic field above 10 T [Fig. 2(a)], implying vanishing SSC in the fully field-aligned collinear Ru spins, as observed in  $\sigma_{xy}$  in the archetypal pyrochlore magnet  $\text{Nd}_2\text{Mo}_2\text{O}_7$  with SSC [29]. Thus,  $S_A$  of  $(\text{Pr}_{1-x}\text{Ca}_x)_2\text{Ru}_2\text{O}_7$  for  $x = 0.4$  can be deduced from the slope of the line connecting the  $\sigma_{xy}$  data points at  $M = 0$  ( $B = 0$  T) and at the saturated  $M$  (e.g.,  $B = 14$  T) in the  $M$ - $\sigma_{xy}$  plot [dashed line in the left panel of Fig. 2(c)]. Note that the 30 K data almost coincide with this relation, meaning the SSC fading at and above this temperature. After subtracting this  $M$ -linear AHE term, the GHE conductivity term  $\sigma_{xy}^G$  is obtained as shown in Fig. 2(d). At 2 K,  $\sigma_{xy}^G$  sharply arises with the magnetic field, has a peak, and gradually vanishes. This is a consequence of the competition between the Zeeman energy favoring the collinear Ru spin alignment and the magnetic anisotropic energy forming the SSC, which stems from the exchange interaction between Ru spins and Ising Pr 4*f* moments. With increasing temperature, the peak value decreases, and its magnetic field value shifts to a higher value, as expected from the thermal fluctuation of the Pr 4*f* moments.

In contrast to the hole-doped paramagnetic-metal regime ( $0.3 \leq x < 0.5$ ), in the electron-doped regime of  $(\text{Pr}_{1-x}\text{Ca}_x)_2\text{Ru}_2\text{O}_7$  ( $0.5 \leq x < 1$ ), the interaction among Ru 4*d* electrons causes the ferromagnetic correlation even at zero field, whereas their coupling to the Pr 4*f* moments causes both 4*d*- and 4*f*-moment-coupled magnetic orders. In this regime, the magnetic transition is discerned from a

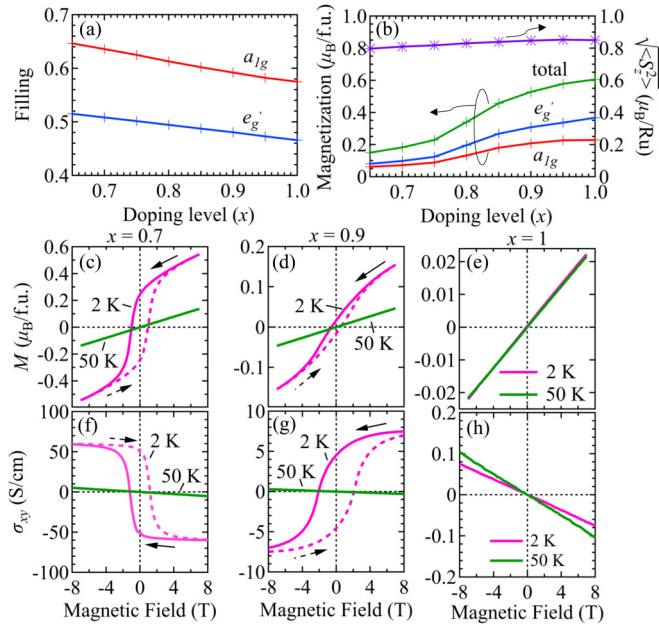


FIG. 3. DFT+DMFT results for (a) the orbital occupancy and (b) magnetization plotted against  $x$ . Red and blue crosses represent the results for  $a_{1g}$  and  $e'_g$  orbitals, respectively. Purple asterisks in (b) represent the expectation value of the local moment  $\sqrt{\langle S_z^2 \rangle}$ . Magnetic field dependence of (c)–(e) magnetization  $M$  and (f)–(h) Hall conductivity  $\sigma_{xy}$  for  $(\text{Pr}_{1-x}\text{Ca}_x)_2\text{Ru}_2\text{O}_7$  ( $x = 0.7, 0.9, 1$ ) at temperatures of 2 and 50 K, below and above  $T_c^*$ , respectively.

bifurcation between the field-cooling and zero-field-cooling curves in the temperature-magnetization measurement. The transition temperature  $T_c^*$  estimated from the magnetization  $M$  is plotted in Fig. 1(d) with black circles. When the temperature is low enough below  $T_c^*$ , the field dependences of  $M$  [Figs. 3(c) and 3(d)] and  $\sigma_{xy}$  [Figs. 3(f) and 3(g)] of  $(\text{Pr}_{1-x}\text{Ca}_x)_2\text{Ru}_2\text{O}_7$  ( $x = 0.7, 0.9$ ) commonly show hysteresis curves, indicating the existence of ferromagnetic domains. The spontaneous magnetization  $M_s$  and the Hall conductivity at 0 and 4 T are plotted in Figs. 4(a) and 4(c), indicating that the ferromagnetic-paramagnetic boundary is located around  $x = 0.5$ . On the other hand, for  $x = 1$  ( $\text{Ca}_2\text{Ru}_2\text{O}_7$ ), where the spin-glass transition has been observed at  $T_N = 25$  K in previous studies [23], no clear hysteresis is observed even at the lowest temperature (2 K), as shown in Figs. 3(e) and 3(h). For all values of  $x$ ,  $M$  does not saturate even at  $B = 7$  T, indicating an antiferromagnetic coupling between the Pr 4*f* moment and Ru 4*d* spin, as observed in the pyrochlore ferromagnet  $\text{Nd}_2\text{Mo}_2\text{O}_7$  [36]. Figure 4(a) plots the Ru moment part of the spontaneous magnetization [ $M_s^{\text{Ru}} = M_s - (-M^{\text{Pr}})$ ] as green squares, as analyzed by assuming the antiferromagnetic *f-d* coupling. Here the Pr moment part of the magnetization is estimated by  $M^{\text{Pr}} = M_{\text{sat}}^{\text{Pr}}(1 - x)$ , where  $M_{\text{sat}}^{\text{Pr}} = (2.5\mu_B/\text{Pr})$  is the saturation magnetism from  $\text{Pr}^{3+}$  moments in a polycrystalline form, which is approximated by  $M$  at  $B = 7$  T for the nondoped  $\text{Pr}_2\text{Ru}_2\text{O}_7$ . The value of  $M_s^{\text{Ru}}$  appears considerably lower than the fully polarized value,  $\sim(4 + 2x)\mu_B/\text{f.u.}$  in the ionic picture, due mostly to the itinerant character of the Ru electrons and due partly to the size effect of the crystal grains. We note that the above assumption of the robustness of the

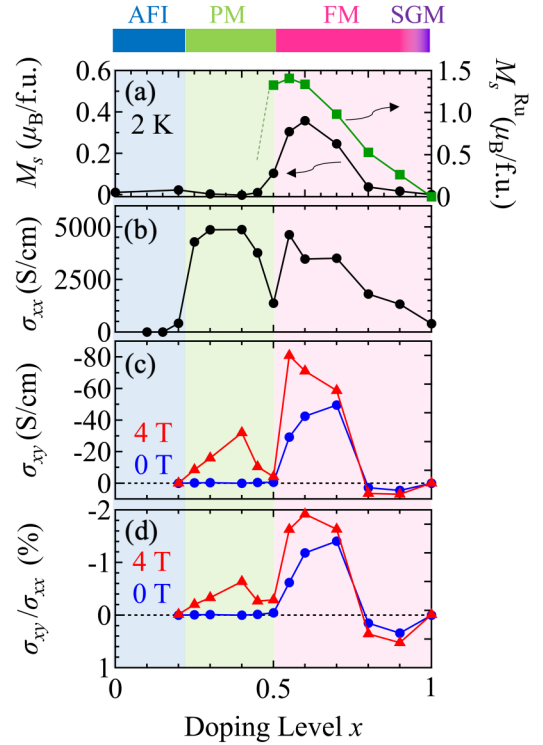


FIG. 4. Doping level  $x$  dependence of (a) spontaneous magnetization  $M_s$ , (b) conductivity  $\sigma_{xx}$ , (c) Hall conductivity  $\sigma_{xy}$ , and (d) Hall angle  $\sigma_{xy}/\sigma_{xx}$  at 2 K. Green squares in (a) show the estimated value of spontaneous magnetization for the Ru 4*d* moment, where the antiferromagnetic *f-d* coupling, such as  $M_s = M_s^{\text{Ru}} - M^{\text{Pr}}$ , is assumed. Shaded colors and the color bar highlight the corresponding electronic and magnetic phases.

Ru ferromagnetism, which is antiferromagnetically coupled with the full Pr magnetization  $M_{\text{sat}}^{\text{Pr}}$ , becomes unjustified in the vicinity of the paramagnetic phase boundary ( $x \sim 0.5$ ), where  $M_s^{\text{Ru}}$  will be overestimated.

To understand the mechanism of ferromagnetism in the electron-doped regime, i.e., the higher- $x$  region near  $\text{Ca}_2\text{Ru}_2\text{O}_7$ , we theoretically investigate the electronic structure of  $(\text{Pr}_{1-x}\text{Ca}_x)_2\text{Ru}_2\text{O}_7$ . The calculation is based on density functional theory combined with the dynamical mean-field theory (DMFT). We find that the DMFT indeed has a ferromagnetic solution for  $0.65 < x \leq 1$ , where  $J_H$  reduces the quasiparticle weight, in line with the Hund's metal picture [26]. Figures 3(a) and 3(b) plot the calculated orbital filling and  $M$  against the doping level  $x$ . The filling of the  $a_{1g}$  and  $e'_g$  orbitals similarly increases with electron doping ( $1 - x$ ) to  $\text{Ca}_2\text{Ru}_2\text{O}_7$ , while the magnetization systematically decreases. Such behaviors suggest that both  $a_{1g}$  and  $e'_g$  orbitals have an itinerant character, unlike a simple double-exchange mechanism which accounts for the distinct roles of the localized  $a_{1g}$  and itinerant  $e'_g$  electrons. Nevertheless, Hund's coupling  $J_H$ , which contributes less to the Stoner mechanism for the itinerant magnetism, plays a crucial role in the present ferromagnetism [37]. This fact is substantiated by the result that the ferromagnetism disappears when we artificially set  $J_H = 0$ . It would also explain the suppression of  $M$  with decreasing  $x$  since  $J_H$  would become less effective from  $\text{Ru}^{5+}$  ( $S = 3/2$ ) to

$\text{Ru}^{4+}$  ( $S = 1$ ). The calculated  $M$  values ( $0.2\mu_B$ - $0.6\mu_B$ /f.u.) are comparable to the experimentally observed values [see Fig. 4(a)] apart from the above-mentioned possible overestimate of the experimental values at  $x = 0.5$ - $0.6$ , close to the paramagnetic-phase boundary. Despite this small  $M$ , the calculated local moment  $\sqrt{\langle S_z^2 \rangle}$  is rather large ( $\sim 0.8\mu_B$ /Ru). This discrepancy would be consistent with the picture that conduction electrons align large local moments fluctuating dynamically. However, the DMFT does not reproduce the experimental  $x$  dependence of  $M$ . In particular, near  $x = 1$ , as evidenced by the experimental observation of the spin-glass phase, the competition between the ferromagnetic and antiferromagnetic interactions as well as the magnetic frustration on the pyrochlore lattice would be necessary to explain this discrepancy.

Finally, we sum up the whole  $x$  dependence of the magnetotransport properties. In the analysis of  $\sigma_{xy}$  in the paramagnetic-metal region of  $(\text{Pr}_{1-x}\text{Ca}_x)_2\text{Ru}_2\text{O}_7$ , we show that the Ising-anisotropic moments of Pr induce the SSC of the Ru spins via the exchange coupling between the Pr  $4f$  moments and the Ru  $4d$  spins, resulting in the GHE. In  $(\text{Pr}_{1-x}\text{Ca}_x)_2\text{Ru}_2\text{O}_7$ , the magnitude of the GHE should be proportional to the probability that the Pr  $4f$  moments form the triad and give finite SSC  $\chi_{ijk} = S_i \cdot (S_j \times S_k)$  on the neighboring  $i$ ,  $j$ , and  $k$  sites and is finite, i.e.,  $(1-x)^3$  [38]. However,  $\sigma_{xy}$  plotted in Fig. 4(c) deviates from the  $(1-x)^3$  dependence, indicating that the intrinsic AHE of SOC origin is not negligible in the magnetotransport of  $(\text{Pr}_{1-x}\text{Ca}_x)_2\text{Ru}_2\text{O}_7$ . The intrinsic AHE, relating to the  $k$ -space Berry curvature, is typically enhanced when the Fermi energy approaches the anticrossing points or Weyl points in the band structure [39,40].

In our case,  $|\sigma_{xy}|$  increases systematically with increasing  $x$  until around  $x = 0.6$ , where the Hall angle lifts up to 2%, and the sign change occurs between  $x = 0.7$  and  $x = 0.8$  [Fig. 4(d)]. This  $x$  dependence of  $\sigma_{xy}$  suggests that the Fermi level may cross one of the Weyl nodes involving a large Berry curvature, along with the carrier doping.

In summary, we investigated the electronic and magnetic properties in mixed crystals of the pyrochlore  $(\text{Pr}_{1-x}\text{Ca}_x)_2\text{Ru}_2\text{O}_7$ , in which the band filling is fully controlled from the  $x = 0$  antiferromagnetic Mott insulator to the  $x = 1$  spin-glass-like correlated bad metal. We found that, as  $x$  increases, the system undergoes a transition from an antiferromagnetic Mott insulator to a paramagnetic metal, where the  $f$ - $d$  coupling between the anisotropic Pr  $4f$  moments and conductive Ru  $4d$  electrons dominates the magnetotransport properties such as the geometrical Hall effect. With further increasing  $x$  above 0.5 or doping electrons to  $\text{Ca}_2\text{Ru}_2\text{O}_7$ , the compounds exhibit metallic ferromagnetism, where the  $4d$  electrons are strongly correlated by the multi-orbital effect, which is typical of Hund's metals. These phase transitions are accompanied by a large anomalous Hall effect with nontrivial  $x$  dependence, highlighting the easily spin-polarized correlated metallic state affected by Hund's coupling.

We thank Y. Kaneko and A. Kikkawa for helpful advice about crystal growth. This work was supported by the Japan Society for the Promotion of Science (KAKENHI; Grant No. 19K14647) from MEXT and by CREST (Grants No. JPMJCR16F1 and No. JPMJCR1874) from the Japan Science and Technology Agency.

- 
- [1] M. Imada, A. Fujimori, and Y. Tokura, *Rev. Mod. Phys.* **70**, 1039 (1998).
- [2] P. A. Lee, N. Nagaosa, and X. G. Wen, *Rev. Mod. Phys.* **78**, 17 (2006).
- [3] Y. Tokura, *Rep. Prog. Phys.* **69**, 797 (2006).
- [4] A. Georges, L. Medici, and J. Mravlje, *Annu. Rev. Condens. Matter Phys.* **4**, 137 (2013).
- [5] X. Deng, K. M. Stadler, K. Haule, A. Weichselbaum, J. V. Delft, and G. Kotliar, *Nat. Commun.* **10**, 2721 (2019).
- [6] P. Werner, E. Gull, M. Troyer, and A. J. Millis, *Phys. Rev. Lett.* **101**, 166405 (2008).
- [7] L. de Medici, J. Mravlje, and A. Georges, *Phys. Rev. Lett.* **107**, 256401 (2011).
- [8] H. T. Dang, J. Mravlje, A. Georges, and A. J. Millis, *Phys. Rev. B* **91**, 195149 (2015).
- [9] Q. Han, H. T. Dang, and A. J. Millis, *Phys. Rev. B* **93**, 155103 (2016).
- [10] Y. Nomura, S. Sakai, and R. Arita, *Phys. Rev. B* **91**, 235107 (2015).
- [11] H. Shinaoka, S. Hoshino, M. Troyer, and P. Werner, *Phys. Rev. Lett.* **115**, 156401 (2015).
- [12] S. Nakatsuji, D. Hall, L. Balicas, Z. Fisk, K. Sugahara, M. Yoshioka, and Y. Maeno, *Phys. Rev. Lett.* **90**, 137202 (2003).
- [13] W. W. Krempa, G. Chen, Y. B. Kim, and L. Balents, *Annu. Rev. Condens. Matter Phys.* **5**, 57 (2014).
- [14] M. Kim, J. Mravlje, M. Ferrero, O. Parcollet, and A. Georges, *Phys. Rev. Lett.* **120**, 126401 (2018).
- [15] J. S. Gardner, M. J. P. Gingras, and J. E. Greedan, *Rev. Mod. Phys.* **82**, 53 (2010).
- [16] N. Taira, M. Wakeshima, and Y. Hinatsu, *J. Phys.: Condens. Matter* **11**, 6983 (1999).
- [17] M. Ito, Y. Yasui, M. Kanada, H. Harashina, S. Yoshii, K. Murata, M. Sato, H. Okumura, and K. Kakurai, *J. Phys. Chem. Solids* **62**, 337 (2001).
- [18] S. T. Ku, D. Kumar, M. R. Lees, W.-T. Lee, R. Aldus, A. Studer, P. Imperia, S. Asai, T. Masuda, S. W. Chen, J. M. Chen, and L. J. Chang, *J. Phys.: Condens. Matter* **30**, 155601 (2018).
- [19] J. Gurgul, M. Rams, Z. Swiatkowska, R. Kmiec, and K. Tomala, *Phys. Rev. B* **75**, 064426 (2007).
- [20] R. Kmiec, Z. Swiatkowska, J. Gurgul, M. Rams, A. Zarzycki, and K. Tomala, *Phys. Rev. B* **74**, 104425 (2006).
- [21] N. Taira, M. Wakeshima, Y. Hinatsu, A. Tobo, and K. Ohoyama, *J. Solid State Chem.* **176**, 165 (2003).
- [22] K. Ueda, T. Oh, B.-J. Yang, R. Kaneko, J. Fujioka, N. Nagaosa, and Y. Tokura, *Nat. Commun.* **8**, 15515 (2017).
- [23] T. Munenaka and H. Sato, *J. Phys. Soc. Jpn.* **75**, 103801 (2006).

- [24] Y. Y. Jiao, J. P. Sun, P. Shahi, Q. Cui, X. H. Yu, Y. Uwatoko, B. S. Wang, J. A. Alonso, H. M. Weng, and J.-G. Cheng, *Phys. Rev. B* **98**, 075118 (2018).
- [25] R. Kaneko, K. Ueda, C. Terakura, and Y. Tokura, *Phys. Rev. B* **102**, 041114(R) (2020).
- [26] See Supplemental Material at <http://link.aps.org/supplemental/10.1103/PhysRevB.103.L201111> for sample growth, data analysis, and calculation details, which include references on experiments [41–43] and calculations [44–55].
- [27] K. Takeda, H. Hidaka, H. Kotegawa, T. C. Kobayashi, K. Shimizu, H. Harima, K. Fujiwara, K. Miyoshi, J. Takeuchi, Y. Ohishi, T. Adachi, M. Takata, E. Nishibori, M. Sakata, T. Watanuki, and O. Shimomura, *Physica B (Amsterdam, Neth.)* **359**, 1312 (2005).
- [28] N. Nagaosa, J. Sinova, S. Onoda, A. H. MacDonald, and N. P. Ong, *Rev. Mod. Phys.* **82**, 1539 (2010).
- [29] Y. Taguchi, Y. Oohara, H. Yoshizawa, N. Nagaosa, and Y. Tokura, *Science* **291**, 2573 (2001).
- [30] M. Lee, W. Kang, Y. Onose, Y. Tokura, and N. P. Ong, *Phys. Rev. Lett.* **102**, 186601 (2009).
- [31] Y. Machida, S. Nakatsuji, S. Onoda, T. Tayama, and T. Sakakibara, *Nature (London)* **463**, 210 (2009).
- [32] W. Wang, M. W. Daniels, Z. Liao, Y. Zhao, J. Wang, G. Koster, G. Rijnders, C.-Z. Chang, D. Xiao, and W. Wu, *Nat. Mater.* **18**, 1054 (2019).
- [33] T. Kurumaji, T. Nakajima, M. Hirschberger, A. Kikkawa, Y. Yamasaki, H. Sagayama, H. Nakao, Y. Taguchi, T.-H. Arima, and Y. Tokura, *Science* **365**, 914 (2019).
- [34] S. Yoshii, S. Iikubo, T. Kageyama, K. Oda, Y. Kondo, K. Murata, and M. Sato, *J. Phys. Soc. Jpn.* **69**, 3777 (2000).
- [35] Y. Machida, S. Nakatsuji, Y. Maeno, T. Tayama, T. Sakakibara, and S. Onoda, *Phys. Rev. Lett.* **98**, 057203 (2007).
- [36] Y. Yasui, S. Iikubo, H. Harashina, T. Kageyama, M. Ito, M. Sato, and K. Kakurai, *J. Phys. Soc. Jpn.* **72**, 865 (2003).
- [37] S. Sakai, R. Arita, and H. Aoki, *Phys. Rev. Lett.* **99**, 216402 (2007).
- [38] K. Ueda, S. Iguchi, T. Suzuki, S. Ishiwata, Y. Taguchi, and Y. Tokura, *Phys. Rev. Lett.* **108**, 156601 (2012).
- [39] Z. Fang, N. Nagaosa, K. S. Takahashi, A. Asamitsu, R. Mathieu, T. Ogasawara, H. Yamada, M. Kawasaki, Y. Tokura, and K. Terakura, *Science* **302**, 92 (2003).
- [40] C. Shekhar, N. Kumar, V. Grinenko, S. Singh, R. Sarkar, H. Luetkens, S.-C. Wu, Y. Zhang, A. C. Komarek, E. Kampert, Y. Skourski, J. Wosnitzer, W. Schnelle, A. McCollam, U. Zeitler, J. Kübler, B. Yan, H. H. Klauss, S. S. P. Parkin, and C. Felser, *Proc. Natl. Acad. Sci. USA* **115**, 9140 (2018).
- [41] Y. Machida, S. Nakatsuji, H. Tonomura, T. Tayama, T. Sakakibara, J. v. Duijn, C. Broholm, and Y. Maeno, *J. Phys. Chem. Solids* **66**, 1435 (2005).
- [42] T. Kondo *et al.*, *Nat. Commun.* **6**, 10042 (2015).
- [43] Y. Yasui, T. Kageyama, T. Moyoshi, M. Soda, M. Sato, and K. Kakurai, *J. Phys. Soc. Jpn.* **75**, 084711 (2006).
- [44] P. Giannozzi *et al.*, *J. Phys.: Condens. Matter* **29**, 465901 (2017).
- [45] D. R. Hamann, *Phys. Rev. B* **88**, 085117 (2013).
- [46] M. van Setten, M. Giantomassi, E. Bousquet, M. Verstraete, D. Hamann, X. Gonze, and G.-M. Rignanese, *Comput. Phys. Commun.* **226**, 39 (2018).
- [47] J. P. Perdew, K. Burke, and M. Ernzerhof, *Phys. Rev. Lett.* **77**, 3865 (1996).
- [48] N. Marzari and D. Vanderbilt, *Phys. Rev. B* **56**, 12847 (1997).
- [49] I. Souza, N. Marzari, and D. Vanderbilt, *Phys. Rev. B* **65**, 035109 (2001).
- [50] K. Nakamura, Y. Yoshimoto, Y. Nomura, T. Tadano, M. Kawamura, T. Kosugi, K. Yoshimi, T. Misawa, and Y. Motoyama, *Comput. Phys. Commun.* **261**, 107781 (2021).
- [51] RESPACK, <https://sites.google.com/view/kazuma7k6r>.
- [52] F. Aryasetiawan, M. Imada, A. Georges, G. Kotliar, S. Biermann, and A. I. Lichtenstein, *Phys. Rev. B* **70**, 195104 (2004).
- [53] E. Sasioglu, C. Friedrich, and S. Blugel, *Phys. Rev. B* **83**, 121101 (2011).
- [54] A. Georges, G. Kotliar, W. Krauth, and M. J. Rozenberg, *Rev. Mod. Phys.* **68**, 13 (1996).
- [55] M. Caffarel and W. Krauth, *Phys. Rev. Lett.* **72**, 1545 (1994).